

# STELLAR MASS AND COLOR DEPENDENCE OF THE THREE-POINT CORRELATION FUNCTION OF GALAXIES IN THE LOCAL UNIVERSE

HONG GUO<sup>1,2,3</sup>, CHENG LI<sup>1</sup>, Y. P. JING<sup>4</sup>, GERHARD BÖRNER<sup>5</sup>

*Draft version May 23, 2018*

## Abstract

The three-point correlation function (3PCF) for galaxies provides an opportunity to measure the non-Gaussianity generated from nonlinear structure formation and also probes information about galaxy formation and evolution that is generally not available from the two-point correlation function (2PCF). We measure the 3PCF of the Sloan Digital Sky Survey DR7 main sample galaxies in both redshift and projected spaces on scales up to  $40 h^{-1}\text{Mpc}$ . We explore the dependence of the 3PCF on galaxy stellar mass and color in order to constrain the formation and evolution for galaxies of different properties. The study of the dependence on these properties also helps better constrain the relation between galaxy stellar mass and color and the properties of their hosting dark-matter halos. We focus on the study of the reduced 3PCF,  $Q$ , defined as the ratio between the 3PCF and the sum of the products of the 2PCFs. We find a very weak stellar mass dependence of  $Q$  in both redshift and projected spaces. On small scales, more massive galaxies tend to have slightly higher amplitudes of  $Q$ . The shape dependence of  $Q$  is also weak on these small scales, regardless of stellar mass and color. The reduced 3PCF has a strong color dependence for the low-mass galaxies, while no significant dependence on color is found for the high-mass galaxies. Low-mass red galaxies have higher amplitudes and stronger shape dependence of the reduced 3PCF than the blue galaxies, implying that these low-mass red galaxies tend to populate filamentary structures. The linear galaxy bias model fails to interpret the color dependence of  $Q$ , emphasizing the importance of a nonvanishing quadratic bias parameter in the correct modeling of the galaxy color distribution.

*Subject headings:* cosmology: observations, galaxies: statistics, large-scale structure of universe

## 1. INTRODUCTION

In the current paradigm of galaxy formation within a merging hierarchy of dark-matter halos, galaxies form when gas is able to cool, condense, and form stars at the centers of dark-matter halos (White & Rees 1978). Galaxy formation thus involves complicated baryonic processes that play crucial roles on galaxy and cluster scales but are poorly understood in many aspects. One of the resulting effects is that the galaxy distribution is biased relative to the dark matter distribution and such biasing depends strongly on both spatial scale and galaxy properties (see e.g., Kaiser 1984; Bardeen et al. 1986). Studies of galaxy distribution are expected to provide powerful constraints on models of galaxy formation and evolution.

It is common to use the two-point correlation function (2PCF),  $\xi(r)$ , to quantify the galaxy clustering in both theories and galaxy surveys (Davis & Geller 1976; Groth & Peebles 1977; Davis et al. 1985, 1988; Hamilton 1988; White et al. 1988; Boerner et al. 1989; Einasto 1991; Park et al. 1994; Loveday et al.

1995; Benoist et al. 1996; Guzzo et al. 1997; Beisbart & Kerscher 2000; Norberg et al. 2001; Zehavi et al. 2002, 2005, 2011; Li et al. 2006a, 2007; Skibba et al. 2006; Wang et al. 2007; Zheng et al. 2007a; Swanson et al. 2008; Watson et al. 2011; Guo et al. 2013). The 2PCF measures the excess probability of finding pairs in the universe. A Gaussian-distributed density field can be fully described by the 2PCF, or its Fourier-space counterpart, the power spectrum. However, non-Gaussianity naturally arises in the nonlinear evolution of the density fluctuation through the mode-coupling of different scales (see e.g., Bernardeau et al. 2002). To quantify the non-Gaussianity and better understand the galaxy distribution, we would require the next-order statistics in the hierarchy of  $N$ -point correlation functions, the three-point correlation function (3PCF),  $\zeta(r_1, r_2, r_3)$ , which can be used to derive the nonlinear galaxy bias. A consequence of the additional information provided by the 3PCF is that we can break the degeneracy of galaxy bias and  $\sigma_8$  (the rms of the matter density field in the  $8 h^{-1}\text{Mpc}$  sphere) in the 2PCF, which also helps constrain the cosmological parameters (Gaztanaga & Frieman 1994; Gaztañaga et al. 2005; Scoccimarro et al. 2001; Verde et al. 2002; Jing & Börner 2004; Zheng 2004; Gaztañaga et al. 2005; Pan & Szapudi 2005; Nishimichi et al. 2007; Ross et al. 2008; Ross & Brunner 2009; Guo & Jing 2009a; Marín 2011; McBride et al. 2011b; Marín et al. 2013; Pollack et al. 2013).

For the study of the 3PCF, it is generally more convenient to introduce the reduced 3PCF,  $Q(r_1, r_2, r_3)$ , de-

<sup>1</sup> Partner Group of the Max Planck Institute for Astrophysics at the Shanghai Astronomical Observatory and Key Laboratory for Research in Galaxies and Cosmology of Chinese Academy of Sciences, Nandan Road 80, Shanghai 200030, China

<sup>2</sup> Department of Astronomy, Case Western Reserve University, OH 44106, USA

<sup>3</sup> Department of Physics and Astronomy, University of Utah, 115 South 1400 East, Salt Lake City, UT 84112, USA

<sup>4</sup> Center for Astronomy and Astrophysics, Physics Department, Shanghai Jiao Tong University, Shanghai 200240, China

<sup>5</sup> Max-Planck-Institut für Astrophysik, Karl-Schwarzschild-Strasse 1, 85748 Garching, Germany

defined as the ratio between the 3PCF and the sum of the products of the 2PCFs,

$$Q(r_1, r_2, r_3) = \frac{\zeta(r_1, r_2, r_3)}{\xi(r_1)\xi(r_2) + \xi(r_2)\xi(r_3) + \xi(r_3)\xi(r_1)} \quad (1)$$

Such a hierarchical scaling ( $\zeta \propto \xi^2$ ) was introduced by [Groth & Peebles \(1977\)](#), assuming  $Q$  to be a constant. Although subsequent theories and observations found that  $Q$  is generally dependent on the size and shape of the triangle  $(r_1, r_2, r_3)$  (see e.g., [Bernardeau et al. 2002](#)), it is still more natural to use  $Q$  as the measurement of non-Gaussianity generated from gravitational clustering. In observation, the redshift-space distortion (RSD) effect will significantly change the shape and amplitude of both the 2PCF and the 3PCF, because the galaxy peculiar velocities prevent us from measuring the real radial distribution of the galaxies. The projected correlation function is then used to minimize the influence of the RSD. Since the projected correlation function can be easily converted to the real-space correlation function ([Davis et al. 1985](#)), the projected 3PCF was proposed to represent the actual 3PCF in real space. [Jing & Börner \(1998\)](#) first applied this statistic to the Las Campanas Redshift Survey.

In order to use the 3PCF to constrain the galaxy formation and evolution models, knowledge of the relation between galaxies and dark-matter halos is important. The clustering dependence of the 2PCF on galaxy properties is extensively investigated in the literature to infer how galaxies of different properties populate the dark-matter halos of different masses, which is commonly referred to as the halo occupation distribution (HOD) (e.g., [Zehavi et al. 2005, 2011](#); [Zheng et al. 2007b, 2009](#); [Coupon et al. 2012](#)). However, the 2PCF itself is not enough to break the degeneracy in the theoretical model parameters. The measurements of the clustering dependence on galaxy properties from the 3PCF will further help put a strong constraint on the allowed HOD parameters ([Kulkarni et al. 2007](#)).

[Jing & Börner \(2004\)](#) used the Two-degree Field Galaxy Redshift Survey (2dFGRS; [Colless et al. 2001](#)) to measure the luminosity dependence of the reduced 3PCF,  $Q(r_1, r_2, r_3)$ , in both redshift and projected spaces. They found a small but significant trend: more luminous galaxies have lower amplitudes of  $Q$ . [Gaztañaga et al. \(2005\)](#) also measured the redshift-space  $Q$  with 2dFGRS and found a weak tendency for  $Q$  to decrease with increasing luminosity in the nonlinear regime. [Kayo et al. \(2004\)](#) and [Nichol et al. \(2006\)](#) employed the early data release of the Sloan Digital Sky Survey (SDSS; [York et al. 2000](#)) and found no significant dependence of  $Q$  on galaxy morphology, color, or luminosity. Considering the large measurement errors, their results are statistically consistent with [Jing & Börner \(2004\)](#) and [Gaztañaga et al. \(2005\)](#). [McBride et al. \(2011a\)](#) explored the dependence of  $Q$  on luminosity and color in redshift and projected spaces using SDSS Data Release 6. They found a similar luminosity and color dependence to previous work and inferred that the weak shape dependence of  $Q$  on small scales is caused by the RSD.

Apart from the analysis of the observational data, another way to study the effect of the RSD on the 3PCF is to use numerical simulations (e.g.,

[Gaztañaga & Scoccimarro 2005](#); [Marín et al. 2008](#)). [Marín et al. \(2008\)](#) used  $N$ -body simulations to construct mock galaxy catalogs and compared  $Q$  in both real and redshift spaces. They found the same luminosity dependence of  $Q$  as in the observations and they argued that the color dependence of  $Q$  appears stronger than the luminosity dependence, which is consistent with the finding of [Gaztañaga et al. \(2005\)](#).

In this paper, we will focus on measuring the dependence of the 3PCF on the galaxy stellar mass and the dependence on color in certain stellar mass bins. We use the final release data (DR7; [Abazajian et al. 2009](#)) of SDSS to measure the 3PCF in both redshift and projected spaces in the local universe. Since the stellar mass dependence of the 3PCF has never been studied before, it will provide powerful constraints on the connection between galaxy stellar mass and their hosting dark matter halo mass, which will be explored in our future work. For consistency with previous work, we also briefly investigate the luminosity dependence of the 3PCF in our sample. We extend the previous analysis by exploring galaxy samples in a broader range of scales and triangle configurations, in order to clarify whether the weak shape dependence of  $Q$  is really caused by the RSD.

The paper is constructed as follows: In Section 2, we briefly describe the galaxy and mock samples. The methods of measuring the 2PCF and 3PCF are presented in Section 3. We present our results of the stellar mass and color dependence of the 3PCF in Section 4. We summarize our results in Section 5.

Throughout this paper we assume a cosmology model with a density parameter  $\Omega_m = 0.3$ , a cosmological constant  $\Omega_\Lambda = 0.7$ , and a Hubble constant  $H_0 = 100h\text{kms}^{-1}\text{Mpc}^{-1}$  with  $h = 1.0$ .

## 2. DATA

### 2.1. SDSS Galaxy Samples

The galaxy sample used in this paper is a magnitude-limited sample taken from the New York University Value-Added Galaxy Catalog (NYU-VAGC), constructed by [Blanton et al. \(2005\)](#) based on SDSS DR7. This sample has formed the basis for the recent studies on the galaxy distribution in the low-redshift universe (e.g., [Li et al. 2012a,b, 2013](#)). The sample contains about half a million galaxies located in the main contiguous area of the survey in the Northern Galactic Cap, with  $r < 17.6$ ,  $-24 < M_r < -16$ , and spectroscopically measured redshifts in the range of  $0.001 < z < 0.5$ . Here  $r$  is the  $r$ -band Petrosian apparent magnitude, corrected for Galactic extinction, and  $M_r$  is the  $r$ -band Petrosian absolute magnitude, corrected for evolution and  $K$ -corrected to  $z = 0.1$ . The apparent magnitude limit is chosen to select a sample that is uniform and complete over the entire area of the survey (see [Tegmark et al. 2004](#)). The median redshift of this sample is  $z = 0.088$ , with 10% of the galaxies below  $z = 0.033$  and 10% above  $z = 0.16$ .

The stellar mass of each galaxy in our sample accompanies the NYU-VAGC release. It is estimated based on the redshift and the five-band Petrosian magnitudes from the SDSS photometric data, as described in detail in [Blanton & Roweis \(2007\)](#). This estimate corrects implicitly for dust and assumes a universal stellar initial mass function (IMF) of [Chabrier \(2003\)](#)

form. As demonstrated in Appendix A of Li & White (2009), once all estimates are adapted to assume the same IMF, the estimated stellar masses agree quite well with those obtained from the simple, single-color estimator of Bell et al. (2003) and also with those derived by Kauffmann et al. (2003) from a combination of SDSS photometry and spectroscopy.

From this sample we select two sets of samples according to either  $r$ -band absolute magnitude ( $M_r$ ) or stellar mass ( $\log M_s$ ). In each of these samples, we further divide the galaxies into *red* and *blue* populations according to their  $g - r$  colors, following the luminosity-dependent color cut determined in Li et al. (2006a). Details of the luminosity- and mass-selected samples, as well as their red/blue samples, are listed in Table 1. The effective volume of each sample is calculated from the summation (e.g., Percival et al. 2010)

$$V_{\text{eff}} = \sum_i \left( \frac{\bar{n}(z_i)P_0}{1 + \bar{n}(z_i)P_0} \right)^2 \Delta V(z_i), \quad (2)$$

where  $\bar{n}(z_i)$  is the mean number density in the volume shell  $\Delta V(z_i)$  at  $z_i$  and  $P_0 = 10^4 h^{-3} \text{Mpc}^3$ . We show the number density distribution,  $n(z)$ , for the different stellar-mass and luminosity subsamples in Figure 1. As expected, more massive or luminous galaxies are spread over a larger volume. The least massive or the faintest subsample only cover a small local volume, and their correlation function measurements may suffer from a significant cosmic variance effect, as will be shown in the following sections.

## 2.2. Random Samples

To obtain reliable estimates of the auto-correlation functions, each observed sample in Table 1 must be compared with a “random sample” that is unclustered but fills the same region of the sky and has the same, position-dependent spectroscopic completeness and luminosity-dependent redshift distribution. We construct our random samples from the observed samples themselves, as described in detail in Li et al. (2006a). For each real galaxy, we generate 10 sky positions at random within the mask of the survey (see Blanton et al. 2005, for details), and we assign to each of them the properties of the real galaxy—in particular, its values of redshift, luminosity, and stellar mass as well as the position-dependent spectroscopic completeness. This method is valid only for wide-field surveys like SDSS, where randomizing sky positions should be sufficient to break the coherence of the large-scale structures in the real sample. Extensive tests show that random samples constructed in this way produce indistinguishable results from those using the traditional method, which relies on the galaxy luminosity function obtained from the same survey to determine the redshift-dependent average number density of galaxies required for generating the random points (Li et al. 2006b).

## 2.3. Mock Galaxy Samples

We construct a set of 80 mock SDSS galaxy catalogs from the Millennium Simulation (Springel et al. 2005) using both the sky mask and the magnitude and redshift limits of our real SDSS sample. The Millennium

Simulation uses  $10^{10}$  particles to follow the dark-matter distribution in a cubic region with  $500h^{-1} \text{Mpc}$  on a side, assuming the concordance  $\Lambda$  cold dark-matter cosmology. Galaxy formation within the evolving dark-matter halos is simulated in postprocessing using semi-analytic methods tuned to give a good representation of the observed low-redshift galaxy population. Our mock catalogs are based on the galaxy formation model of Croton et al. (2006) and are constructed from the publicly available data at  $z = 0$  using the methodology of Li et al. (2006b) and Li et al. (2007). These mock catalogs allow us to derive reasonable error estimates for the correlation functions we measure, including both sampling and cosmic-variance uncertainties. We use all 80 mock catalogs for estimating the errors of our 2PCF measurements. For the 3PCFs, we use only 10 of the 80 mock catalogs randomly selected from the whole set, in order to save computational time while obtaining a reasonably good estimation of the errors. The volume of the Millennium simulation is  $0.125h^{-3} \text{Gpc}^3$ , which is enough for most of our stellar mass and luminosity subsamples, and only slightly smaller than those of the samples  $M4$  and  $L4$  (see Table 1). We note that the error estimation in this paper makes use of only the diagonal elements of the covariance matrix of the mock catalogues, and so the errors on different scales for a given sample are correlated to varying degrees. However, we argue that this is not an issue in our case where we use these errors mainly to indicate the relative differences in the 2PCF and the 3PCF measured at given scale between different samples. We also note that the possible systematic errors in our estimation of the galaxy stellar mass and also the photometric errors in the galaxy color are not considered. These errors would not change our conclusions of the dependence on galaxy properties since they would not significantly mix the galaxy samples.

## 3. CORRELATION FUNCTION MEASUREMENTS

### 3.1. Two-point Correlation Function

We begin by estimating the two-dimensional, redshift-space, two-point auto-correlation function,  $\xi(r_p, r_\pi)$ , for each of the samples listed in Table 1 using the estimator of Landy & Szalay (1993):

$$\xi(r_p, r_\pi) = \frac{\text{DD} - 2\text{DR} + \text{RR}}{\text{RR}}, \quad (3)$$

where DD, DR, and RR are the data-data, data-random and random-random pair counts, and  $r_p$  and  $r_\pi$  are the pair separations perpendicular and parallel to the line of sight. To normalize appropriately, RR needs to be multiplied by  $(N_g/N_r)^2$  and DR by  $N_g/N_r$ , where  $N_g$  and  $N_r$  are the numbers of galaxies in the real and random samples, respectively. In our case,  $N_r = 10 \times N_g$ . We have corrected the effect of fiber collisions in the same way as in Li et al. (2006b) and Li et al. (2007). Briefly, we up-weight each galaxy pair separated by angular distance  $\theta$  by the ratio  $F(\theta) = [1 + w_{pz}(\theta)]/[1 + w_{sz}(\theta)]$ , where  $w_{sz}(\theta)$  and  $w_{pz}(\theta)$  are the angular 2PCFs of the spectroscopic and the parent photometric samples, respectively. Detailed tests of the method can be found in Li et al. (2006b) and Guo et al. (2012).

Next, we integrate these two-dimensional correlation estimates over the line-of-sight separation  $r_\pi$  to obtain

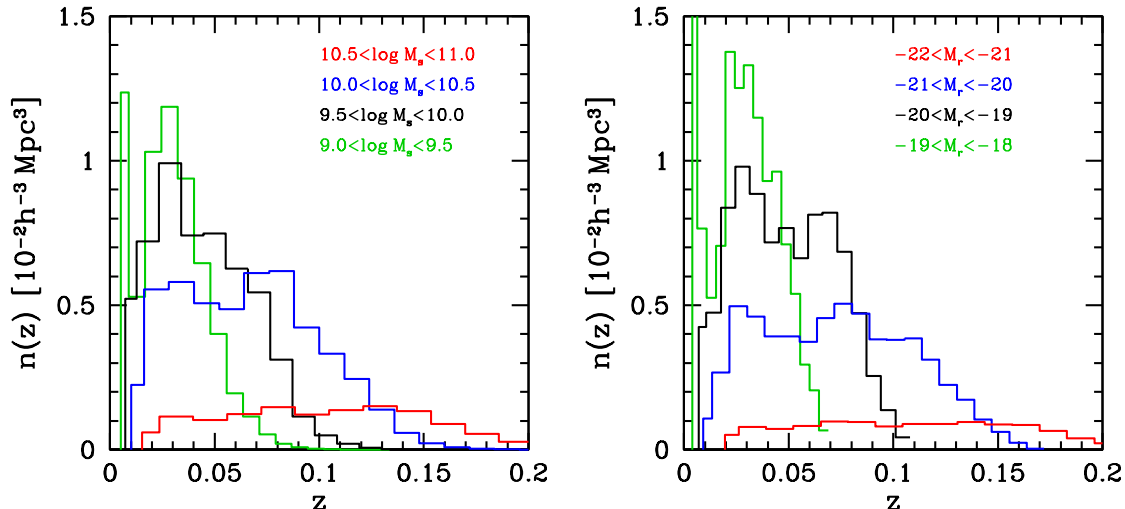


FIG. 1.— Number density distribution for stellar mass (left panel) and luminosity subsamples (right panel). (A color version of this figure is available in the online journal.)

TABLE 1  
FLUX-LIMITED SAMPLES OF DIFFERENT LUMINOSITY AND STELLAR MASS

| Sample | $\log(M_s)$ | $\bar{z}$ | $V_{\text{eff}}$ | Number of Galaxies | Red Galaxies | Blue Galaxies |
|--------|-------------|-----------|------------------|--------------------|--------------|---------------|
| M1     | [9.0, 9.5)  | 0.046     | 0.011            | 32573              | 6658         | 25915         |
| M2     | [9.5, 10)   | 0.066     | 0.028            | 84024              | 30700        | 53324         |
| M3     | [10, 10.5)  | 0.095     | 0.069            | 181865             | 97918        | 83947         |
| M4     | [10.5, 11)  | 0.137     | 0.129            | 143235             | 99932        | 43303         |
| Sample | $M_r$       | $\bar{z}$ | $V_{\text{eff}}$ | Number of Galaxies | Red Galaxies | Blue Galaxies |
| L1     | [-19, -18)  | 0.042     | 0.006            | 36223              | 13127        | 23096         |
| L2     | [-20, -19)  | 0.067     | 0.022            | 107241             | 52169        | 55072         |
| L3     | [-21, -20)  | 0.102     | 0.070            | 189880             | 102128       | 87752         |
| L4     | [-22, -21)  | 0.147     | 0.136            | 118728             | 73002        | 45726         |

NOTE. — The stellar mass  $M_s$  is in units of  $h^2 M_\odot$ , where we assume  $h \equiv 1$  throughout the paper. The effective volume  $V_{\text{eff}}$  is in units of  $h^{-3} \text{Gpc}^3$ .

the projected auto-correlation function,  $w_p(r_p)$ , as follows,

$$w_p(r_p) = \int_{-r_{\pi, \text{max}}}^{+r_{\pi, \text{max}}} \xi(r_p, r_\pi) dr_\pi = \sum_i \xi(r_p, r_\pi) \Delta r_{\pi, i}, \quad (4)$$

where we choose  $r_{\pi, \text{max}} = 40h^{-1} \text{Mpc}$  as the outer limit for the integration depth (in order to reduce the noise from distant uncorrelated regions) so that the summation for computing  $w_p(r_p)$  runs from  $r_{\pi, 1} = -39.5h^{-1} \text{Mpc}$  to  $r_{\pi, 80} = 39.5h^{-1} \text{Mpc}$ , given that we use bins of width  $\Delta r_{\pi, i} = 1h^{-1} \text{Mpc}$ .

In addition to  $w_p(r_p)$ , we also measure the one-dimensional auto-correlation function in redshift space,  $\xi(s)$ , using the same estimator as in Equation (3) but as a function of  $s$ , the redshift-space three-dimensional (3D) pair separation, which is given by  $s^2 = r_p^2 + r_\pi^2$ .

In Figure 2, we present the measurements of  $w_p(r_p)$  (top panels) and  $\xi(s)$  (bottom panels) for the four stellar-mass-selected samples and also the color subsamples. The errors are estimated from the 80 mock catalogs as described in the previous section. We note that the stellar-mass sample of  $9 < \log M_s < 9.5$  shows a significantly different trend from all other samples. It is caused by the large cosmic variance due to its small volume, which can also be inferred from its small mean

redshift,  $\bar{z} = 0.046$ . Similar behavior is also found for faint galaxies in the luminosity bin of  $-19 < M_r < -18$  (Zehavi et al. 2011), which has a similar mean redshift as this sample. Therefore, in order to better constrain the dependence of the reduced 3PCFs on the stellar mass, we will ignore this sample in the following sections. In all other cases, both  $w_p(r_p)$  and  $\xi(s)$  show systematic trends with galaxy stellar mass, reflecting the different masses of the hosting halos, with more massive galaxies residing in more massive halos (e.g. Wang & Jing 2010). This trend is shown more clearly in the blue subsamples. Because most of the blue galaxies of these stellar masses are central galaxies, the different hosting-halo masses will have stronger effects on the amplitudes of  $w_p(r_p)$ . On the contrary, the two less massive red-galaxy samples ( $\log M_s < 10.0$ ) show strong small-scale clustering. It can be caused by their high satellite fractions that increase the clustering amplitude, though they are located in lower-mass halos (Li et al. 2007; Zehavi et al. 2011).

The contribution to the projected 2PCF can be decomposed into two components: a steeper inner part at pair separations below  $\sim 1h^{-1} \text{Mpc}$  and a flatter outer part at larger separations. In the language of the ‘‘halo model’’ (see, e.g., Cooray & Sheth 2002), the inner part is called the *one-halo* term, where the pair counts are mostly galaxy pairs in the same halo, and the outer part is referred to as the *two-halo* term, where galaxy pairs are



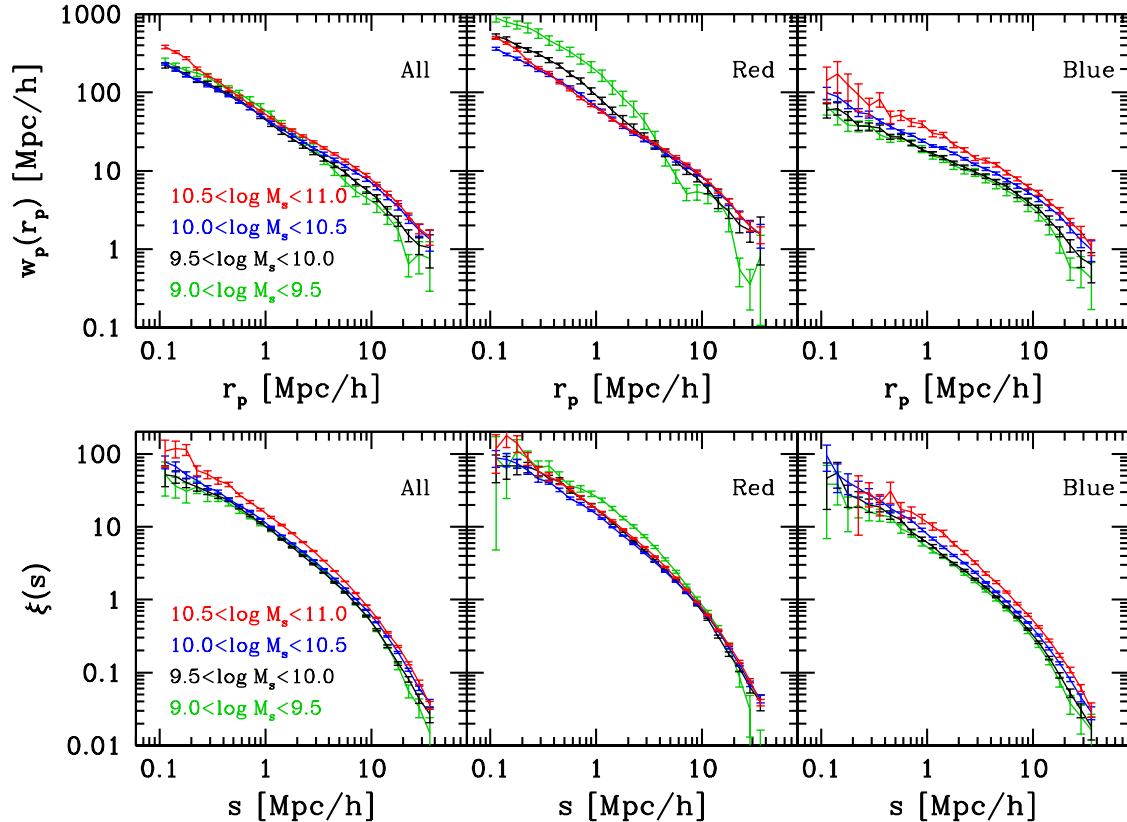


FIG. 2.— Projected- (top panels) and redshift-space (bottom panels) 2PCFs for different stellar-mass samples. Lines of different color denote different stellar samples. The measurements of all the galaxies in each sample are shown in the left panels. The corresponding correlation functions for the red and blue subsamples are also shown in the middle and right panels, respectively. (A color version of this figure is available in the online journal.)

mostly from two separate halos. The separation, where the transition between the two terms occurs, increases with increasing stellar mass. In the two-halo term, the amplitude of  $w_p(r_p)$  is an increasing function of stellar mass, while its slope shows weak or no stellar mass dependence. This is consistent with the picture that, on large scales, the bias in the galaxy distribution is related in a simple way to the bias in the distribution of dark matter halos. When compared to the projected correlation function, the  $\xi(s)$  measurements are relatively suppressed on small scales, leading to almost no transition between the one-halo and two-halo terms. This is caused by the RSD effect on small scales and the global infall toward high-density regions on large scales.

Both the projected and redshift-space 2PCFs have been extensively studied in the literature using both SDSS-based samples (see e.g., Zehavi et al. 2005, 2011; Li et al. 2006a; Guo et al. 2013) and samples from other surveys. Our measurements are well consistent with those previous determinations. In the current paper, these two-point autocorrelation measurements for different stellar mass and color bins will be used in what follows to determine the reduced 3PCFs.

To quantify the galaxy bias of the different stellar-mass samples, we measure the relative bias of the stellar-mass samples to the sample M3 as

$$b/b_{M3} = \sqrt{\xi(r)/\xi_{M3}(r)}, \quad (5)$$

where the 2PCF,  $\xi(r)$ , can be the redshift-space 2PCF

$\xi(s)$  or the projected-space 2PCF  $w_p(r_p)$ . We show in Figure 3 the measurements of the relative bias for the projected - (left panel) and redshift-space (right panel) 2PCFs. Different symbols represent different stellar-mass subsamples, with triangles for  $10.5 < \log M_s < 11$  and circles for  $9.5 < \log M_s < 10$ . As shown, the relative bias is strongly scale dependent for scales less than  $20 h^{-1} \text{Mpc}$ , which reflects the different spatial distributions of the stellar mass subsamples on these nonlinear scales.

### 3.2. Three-point Correlation Function

By analogy with the case of the 2PCF, the definition of the 3PCF in the projected space requires five free parameters,  $r_{p12}$ ,  $r_{p23}$ ,  $r_{p31}$ ,  $r_{\pi12}$ , and  $r_{\pi23}$ , where  $r_{pij}$  and  $r_{\pi ij}$  are the separations of objects  $i$  and  $j$  perpendicular to and along the line of sight. The physical explanation of the 3PCF  $\zeta(r_{p12}, r_{p23}, r_{p31}, r_{\pi12}, r_{\pi23})$  is the excess probability of finding three objects simultaneously in three volume elements  $dV_1$ ,  $dV_2$ , and  $dV_3$  at positions  $\mathbf{s}_1$ ,  $\mathbf{s}_2$  and  $\mathbf{s}_3$ , excluding the contributions from the 2PCFs,

$$\begin{aligned} dp_{123} = & \bar{n}(\mathbf{s}_1)\bar{n}(\mathbf{s}_2)\bar{n}(\mathbf{s}_3) \\ & \times [1 + \xi(r_{p12}, r_{\pi12}) + \xi(r_{p23}, r_{\pi23}) + \xi(r_{p31}, r_{\pi31}) \\ & + \zeta(r_{p12}, r_{p23}, r_{p31}, r_{\pi12}, r_{\pi23})] dV_1 dV_2 dV_3. \quad (6) \end{aligned}$$

The projected 3PCF  $\Pi(r_{p12}, r_{p23}, r_{p31})$  and its reduced counterpart  $Q_p(r_{p12}, r_{p23}, r_{p31})$  are defined as

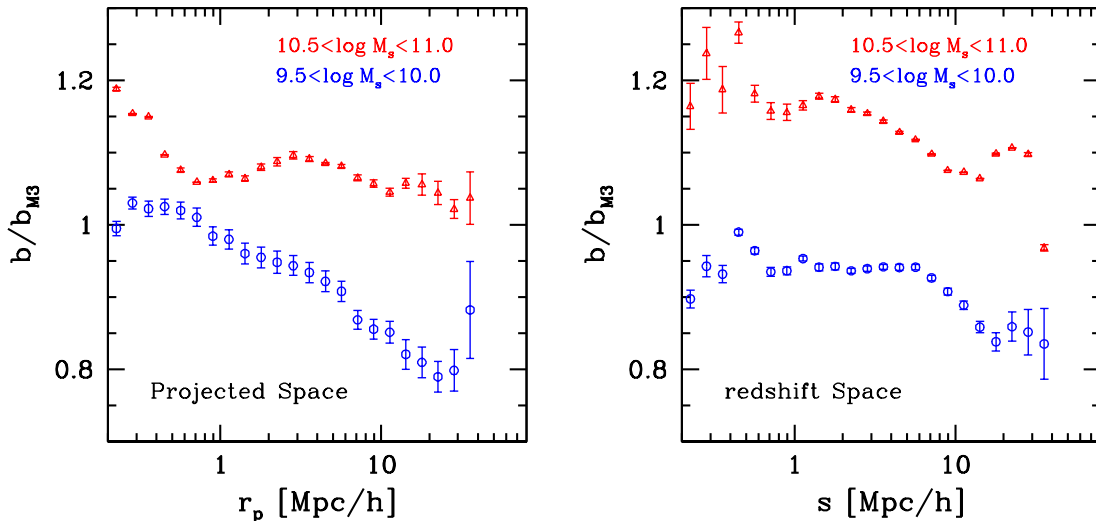


FIG. 3.— Measurements of relative galaxy bias,  $b/b_{M3}$ , (Equation (5)) for the different stellar mass subsamples, with triangles for  $10.5 < \log M_s < 11$  and circles for  $9.5 < \log M_s < 10$ . The measurements for the projected and redshift space are shown in the left and right panels, respectively. (A color version of this figure is available in the online journal.)

(Jing & Börner 1998, 2004)

$$\Pi(r_{p12}, r_{p23}, r_{p31}) = \int \zeta(r_{p12}, r_{p23}, r_{p31}, r_{\pi12}, r_{\pi23}) dr_{\pi12} dr_{\pi23} \quad (7)$$

$$Q_p(r_{p12}, r_{p23}, r_{p31}) = \frac{\Pi(r_{p12}, r_{p23}, r_{p31})}{w_p(r_{p12})w_p(r_{p23}) + \text{cyc}}. \quad (8)$$

Similarly, the redshift-space reduced 3PCF is defined by

$$Q_s(s_{12}, s_{23}, s_{31}) = \frac{\zeta(s_{12}, s_{23}, s_{31})}{\xi(s_{12})\xi(s_{23}) + \text{cyc}}. \quad (9)$$

We use the following estimator to measure  $\zeta$  and  $\Pi$  in our samples (Szapudi & Szalay 1998),

$$\zeta = \frac{\text{DDD} - 3\text{DDR} + 3\text{DRR} - \text{RRR}}{\text{RRR}}, \quad (10)$$

where DDD, DDR, DRR, and RRR are the normalized number counts of triplets in each bin measured from the data (represented by D) and random samples (represented by R). We correct the fiber-collision effect by adding the weight of each fiber-collided galaxy to its nearest neighbor, which should produce the correct clustering amplitude beyond the fiber-collision scale ( $\sim 0.1 h^{-1} \text{Mpc}$  at  $z \sim 0.1$ ; Guo et al. 2012).

Instead of using  $(r_1, r_2, r_3)$  to represent the triangle, we use the parameterization of  $(r_1, r_2, \theta)$ , with  $r_2 \geq r_1$  and  $\theta = \arccos[(r_1^2 + r_2^2 - r_3^2)/2r_1r_2]$ . We note that in this parameterization, one triangle is counted three times in different bins of  $(r_1, r_2, \theta)$ , but that does not affect our measurements of the configuration dependence. Following Jing & Börner (2004), we use a linear binning scheme for  $\theta$ . The choice of  $\Delta\theta$  is  $\Delta\theta = \pi/20$ , which is small enough to trace the dependence on  $\theta$ . Unless a very large bin size (e.g.,  $\Delta\theta = \pi/5$ ) is used, decreasing the bin size of  $\theta$  in our samples does not improve the results but only reduces the signal-to-noise ratio (S/N; Marin 2011).

As in the 2PCF, we use the same logarithmic binning schemes for  $r_1$  and  $r_2$ , i.e.  $\Delta \log r_1 = \Delta \log r_2$ . In order to

have a reasonable S/N, we use a different  $\Delta \log r_1$  on different scales, but the comparisons of the reduced 3PCF,  $Q$ , for galaxies of different properties are made under the same binning scheme. We note that the amplitude and shape of  $Q$  is coupled with the choice of bin sizes for  $r_1$  and  $r_2$ , because the reduced 3PCF,  $Q$ , is generally dependent on the scale. The range of  $r_3$  for the same angular separation  $\theta$  would also vary with  $\Delta \log r_1$ . For example, for certain  $r_1$  and  $r_2$ , if a very large  $\Delta \log r_1$  is adopted, the values of  $Q(r_1, r_2, \theta)$  are then effectively smoothing over a large range of scales, which may change its shape dependence. So in this paper, we use a small-as-possible  $\Delta \log r_1$  when a reasonable S/N is achieved.

Another commonly used parameterization of  $Q$  is  $(r, u, \theta)$ , where  $r \equiv r_1$ ,  $u \equiv r_2/r_1$ , and  $\theta$  is the angle between  $r_1$  and  $r_2$  (e.g., Scoccimarro et al. 2001; Kayo et al. 2004; Nichol et al. 2006; Kulkarni et al. 2007; Guo & Jing 2009b). The definition is similar to ours, except for the replacement of  $r_2$  by  $u$ . Such a parameterization is introduced to decompose the elements of the triangle into scale (denoted by  $r$ ) and shape (represented by  $u$  and  $\theta$ ) components. We note that in this parameterization,  $\Delta \log r_2 = \Delta \log r_1 + \Delta \log u$ , which means that the bin width of  $r_2$  is always larger than that of  $r_1$ . Including  $u$  complicates the analysis, because we also need to take into account the bin width of  $u$ . In order to have a small enough bin width, we would rather use  $r_2$  instead of  $u$  and require that  $\Delta \log r_2 = \Delta \log r_1$ , which cannot be achieved with the parameterization of  $(r, u, \theta)$ .

To find a suitable  $r_{\pi, \text{max}}$  for the integration of the 3PCF  $\zeta(r_1, r_2, \theta, r_{\pi1}, r_{\pi2})$  along the line of sight, we investigate its effect using the stellar-mass sample M3, which is the largest stellar-mass subsample. The measurements of projected 3PCF,  $Q_p$ , using different  $r_{\pi, \text{max}}$  for the real data and mocks are shown in the top left and top right panels of Figure 4, respectively. In the calculation of  $Q_p$ , the  $r_{\pi, \text{max}}$  for both  $\Pi(r_1, r_2, r_3)$  and  $w_p(r_p)$  are kept the same in order to test its effect. It is clear that the amplitude and shape of  $Q_p$  are depen-

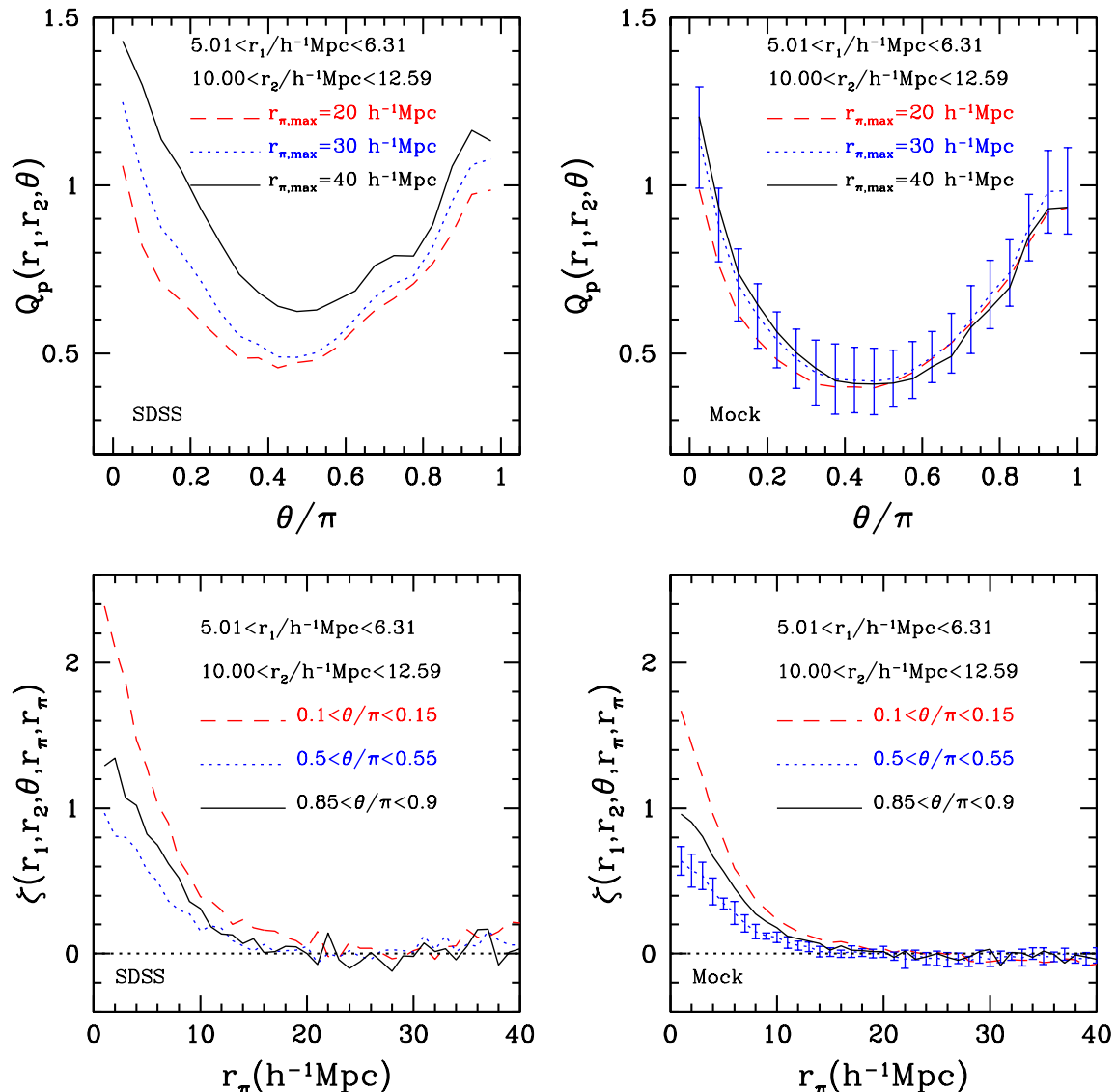


FIG. 4.— Top panels: measurements of projected 3PCF,  $Q_p(r_1, r_2, \theta)$ , using  $r_{\pi, \max} = 20 \text{ h}^{-1} \text{ Mpc}$  (red dashed lines),  $30 \text{ h}^{-1} \text{ Mpc}$  (blue dotted lines), and  $40 \text{ h}^{-1} \text{ Mpc}$  (black solid lines) for the real data (left) and mocks (right). The measurements are made for the stellar-mass subsample  $10 < \log M_s < 10.5$ , and in specific cases of  $r_1$  and  $r_2$ . The measurement errors for the mocks are only shown for one sample for clarity. Bottom panels: data (left) and mock (right) measurements of  $\zeta(r_1, r_2, \theta, r_{\pi 1}, r_{\pi 2})$  for the case of  $r_{\pi 1} = r_{\pi 2}$  in the same ranges of  $r_1$  and  $r_2$  but three different ranges of  $\theta$ , denoted by different types of lines as labeled. (A color version of this figure is available in the online journal.)

dent on the choice of  $r_{\pi, \max}$ , consistent with the conclusions of McBride et al. (2011a). We find that the mocks provide reasonably good consistency with the real data when  $r_{\pi, \max} = 20 \text{ h}^{-1} \text{ Mpc}$  is used. However, the  $Q_p$  of the real data is significantly larger than the mock predictions when a larger  $r_{\pi, \max}$  is employed.

To investigate this further, we show in the bottom panels of Figure 4 the measurements of  $\zeta(r_1, r_2, \theta, r_{\pi 1}, r_{\pi 2})$  for the case of  $r_{\pi 1} = r_{\pi 2}$  in specific ranges of  $r_1$ ,  $r_2$ , and  $\theta$  as labeled in the figure. As shown in the real data, most of the signals are included within  $r_{\pi, \max} = 20 \text{ h}^{-1} \text{ Mpc}$  and the measurements beyond  $r_{\pi, \max} = 20 \text{ h}^{-1} \text{ Mpc}$  are mostly contributed to by the noise of uncorrelated triplets. However, such noise is not well reproduced in the mocks. So in order to have a reasonable estimate of the errors, as well as suppressing the contribution from the noise, we set the maximum of integration over the

line of sight as  $r_{\pi, \max} = 20 \text{ h}^{-1} \text{ Mpc}$  for both  $r_{\pi 12}$  and  $r_{\pi 23}$ , the same as in McBride et al. (2011a). Changing  $r_{\pi, \max}$  for the 2PCF from  $40 \text{ h}^{-1} \text{ Mpc}$  to  $20 \text{ h}^{-1} \text{ Mpc}$  will only have effects at a few percent level. So we still use the measurements of the 2PCFs from the integrations to  $40 \text{ h}^{-1} \text{ Mpc}$  along the line of sight. The binning of  $r_{\pi}$  is defined as  $\Delta r_{\pi} = 1 \text{ h}^{-1} \text{ Mpc}$ , the same as in Jing & Börner (2004). The choice of  $\Delta r_{\pi}$  will only significantly affect the resulting correlation functions when a very large bin size is used (McBride et al. 2011a). The possible noise produced by null random triplet counts in  $r_{\pi}$  bins is reduced by requiring  $\zeta = 0$  in such bins to ignore their contributions. The resulting projected 3PCF will not be significantly affected when a large random sample is used.

#### 4.1. Stellar-mass Dependence

Before exploring the stellar-mass dependence of the 3PCF, we show in Figure 5 the luminosity dependence of  $Q_s$  in redshift space and  $Q_p$  in projected space for comparison with other work (e.g. McBride et al. 2011a). For simplicity and without loss of generality, we only show  $Q_s$  and  $Q_p$  for the configuration of  $\bar{r}_2/\bar{r}_1 = 2$ . Lines of different colors denote different luminosity samples, with the black solid, blue dotted, and red dashed lines for  $L2$ ,  $L3$ , and  $L4$ , respectively (from faint samples to luminous ones). The sample  $L1$  is not shown due to its small volume, as explained in Section 3.1. There is a clear luminosity dependence of  $Q_s$  and  $Q_p$ , with more luminous galaxies showing lower  $Q$ , consistent with the findings of Jing & Börner (2004), Gaztañaga et al. (2005) and McBride et al. (2011a). Such dependence is weaker on large scales where the errors on the measurements are also large.

We show in Figure 6 the stellar-mass dependence of the redshift-space reduced 3PCF,  $Q_s$ . Lines of different colors denote samples of different stellar mass, with the black solid, blue dotted, and red dashed lines for  $M2$ ,  $M3$ , and  $M4$  (from low mass to high mass), respectively. Different panels present the results of  $Q_s$  for different scales and shapes. The stellar-mass dependence of  $Q_s$  is very weak, compared with the luminosity dependence. The stellar-mass dependence mostly shows up on small scales, where there is a trend that more massive galaxies have a lower amplitude of  $Q_s$ . This is roughly consistent with the finding that more luminous galaxies have a smaller  $Q_s$  (Jing & Börner 2004; McBride et al. 2011a), considering the strong correlation of stellar mass and luminosity (see e.g., Figure 2 in Li et al. 2006a).

A way to characterize the dependence of 3PCF on stellar mass is to compare the redshift-space 3PCF,  $\zeta(r_1, r_2, \theta)$ , rather than the reduced value,  $Q_s$ . We show in Figure 7 the stellar-mass dependence of  $\zeta(r_1, r_2, \theta)$  for the case of  $\bar{r}_2 = 2\bar{r}_1$  at four different scales. We find that more massive galaxies are clustered more strongly than the less massive ones in the 3PCF, consistent with the results of the 2PCF (Li et al. 2006a). Such a stellar-mass dependence of  $\zeta$  is contrary to the stellar-mass dependence of  $Q_s$ , because the stellar-mass dependence of  $\xi^2$  in Equation (9) is much stronger than that of  $\zeta$ . This can be understood from the larger galaxy bias of those more massive galaxies. In the second-order perturbation theory, the galaxy 3PCF  $\zeta(r_1, r_2, r_3)$  can be expressed as (see e.g., Fry & Gaztanaga 1993; Pan & Szapudi 2005; McBride et al. 2011b; Marín et al. 2013)

$$\zeta = b_1^3 \zeta_m + b_2 b_1^2 (\xi_{m,1} \xi_{m,2} + \xi_{m,2} \xi_{m,3} + \xi_{m,3} \xi_{m,1}), \quad (11)$$

where  $\zeta_m(r_1, r_2, r_3)$  is the dark-matter 3PCF, and  $\xi_{m,i}(r_i)$  is the dark-matter 2PCF at separation  $r_i$ . The parameters  $b_1$  and  $b_2$  are the linear and nonlinear bias factors. To leading order, we can approximate the galaxy 3PCF as  $\zeta \sim b_1^3 \zeta_m$ . Since the galaxy 2PCF,  $\xi$ , scales as  $\xi \sim b_1^2 \xi_m$ , we conclude that  $\xi^2$  varies much stronger ( $\propto b_1^4$ ) with different stellar-mass samples than  $\zeta$ .

When assuming constant galaxy biases  $b_1$  and  $b_2$ , the natural derivation from Equation (11) is (see, e.g., Bernardeau et al. 2002)

$$Q_g = \frac{Q_m}{b_1} + \frac{b_2}{b_1^2}, \quad (12)$$

where  $Q_g$  and  $Q_m$  are the galaxy and dark-matter reduced 3PCFs, respectively. In the linear bias model where  $b_2 = 0$ ,  $Q_g$  is proportional to  $1/b_1$ , consistent with the trend shown in Figure 6. However, such explanations of the dependence of the reduced 3PCF,  $Q_s$ , on the stellar mass are only qualitative, since the galaxy bias on these nonlinear scales is strongly scale dependent, as shown in Figure 3. Moreover, when using the redshift-space 3PCF to measure the galaxy bias, the RSD effect should be carefully taken into account (Scoccimarro et al. 1999; Pan & Szapudi 2005). We will explore the stellar-mass dependence of the 3PCF in more detail using the halo-occupation models in a companion paper.

In the left panels of Figure 6, we find that  $Q_s$  shows a weaker shape dependence on small scales ( $< 2 h^{-1} \text{Mpc}$ ), regardless of the stellar mass. McBride et al. (2011a) measured  $Q_s$  on scales from  $3 h^{-1} \text{Mpc}$  to  $27 h^{-1} \text{Mpc}$  and found significant configuration dependence, consistent with our measurements on similar scales. In order to identify the correct scale of the triangle, we define the scale  $r_{\text{max}}$  as the maximum of  $(r_1, r_2, r_3)$ . Our measurements on these small scales show that the clustering hierarchy,  $\zeta \propto \xi^2$ , would be more accurate when applied on small scales.

Comparing Figures 6 and 7, we find that while  $\zeta$  decreases with the scale, the scale dependence of  $Q_s$  is twofold. For elongated triangle shapes ( $\theta \sim 0$  and  $\pi$ ),  $Q_s$  increases with scale, while for the perpendicular triangles ( $\theta \sim \pi/2$ ), there is a weak trend for  $Q_s$  to decrease as the scale increases. These two effects make  $Q_s$  show a much stronger shape dependence on larger scales. On large scales, galaxies tend to be more clustered in linear structures, such as filaments (Scoccimarro et al. 2001). Less massive galaxies have a stronger shape dependence and are thus possibly more abundant in these linear structures. Since galaxies of different stellar mass generally have different shapes of the 2PCF (Li et al. 2006a), it is indeed expected to find the degeneracy of the stellar-mass and shape dependence on large scales.

The case  $r_1 = r_2$  for  $Q_s$  is very special, because it shows a quite different configuration dependence as in other panels. With such triangles, the 3PCF can measure scales less than  $r_1$  when  $\theta < \pi/3$  and the maximum scale  $r_{\text{max}}$  of the triangle is  $r_1$ . It seems that the configuration dependence of  $Q_s$  shown in this way is determined by  $r_{\text{max}}$  of the triangle. If we define  $r_{\text{max}}$  as the scale, we can use the angle  $\theta_{\text{max}}$  subtended by  $r_{\text{max}}$  as the configuration  $\theta$ . Therefore, the mild shape dependence of  $Q_s$  seen in the top panels of Figure 6 when  $\theta < \pi/3$  is caused by the fact that the  $\theta_{\text{max}}$  subtended by  $r_{\text{max}}$  is only in the range of  $[\pi/3, \pi/2]$ , where the variation of  $Q_s$  with  $\theta_{\text{max}}$  is small. So the shape dependence of  $Q_s$  is correlated with, but not determined by, its scale dependence. The downturn of signals in the first one or two bins ( $\theta \sim 0$ ) in the top panels of Figure 6 can be caused by low S/N of small numbers of triplet counts or by the residual fiber-collision effect since the fiber collision in our measurements is not well corrected below the fiber-collision scale ( $\sim 0.1 h^{-1} \text{Mpc}$ ).

We present the stellar-mass dependence for the projected-space reduced 3PCF,  $Q_p(r_1, r_2, \theta)$ , in Figure 8. Similar to the reduced 3PCF,  $Q_s$ , in redshift space,  $Q_p$  does not have a strong stellar-mass dependence, im-



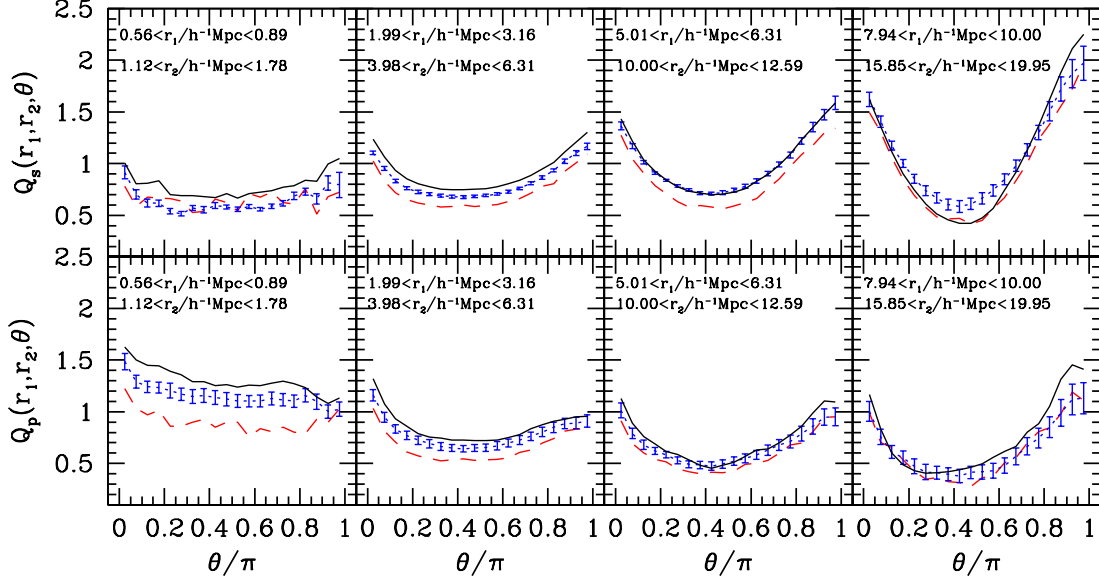


FIG. 5.— Reduced 3PCF in redshift (upper panels) and projected spaces (bottom panels) at different scales and triangle shapes. They are only shown for the case of  $\bar{r}_2 = 2\bar{r}_1$ . Lines of different colors denote different luminosity samples, with the black solid, blue dotted, and red dashed lines for  $L_2$ ,  $L_3$ , and  $L_4$ , respectively. The errors are only shown for one sample for clarity. (A color version of this figure is available in the online journal.)

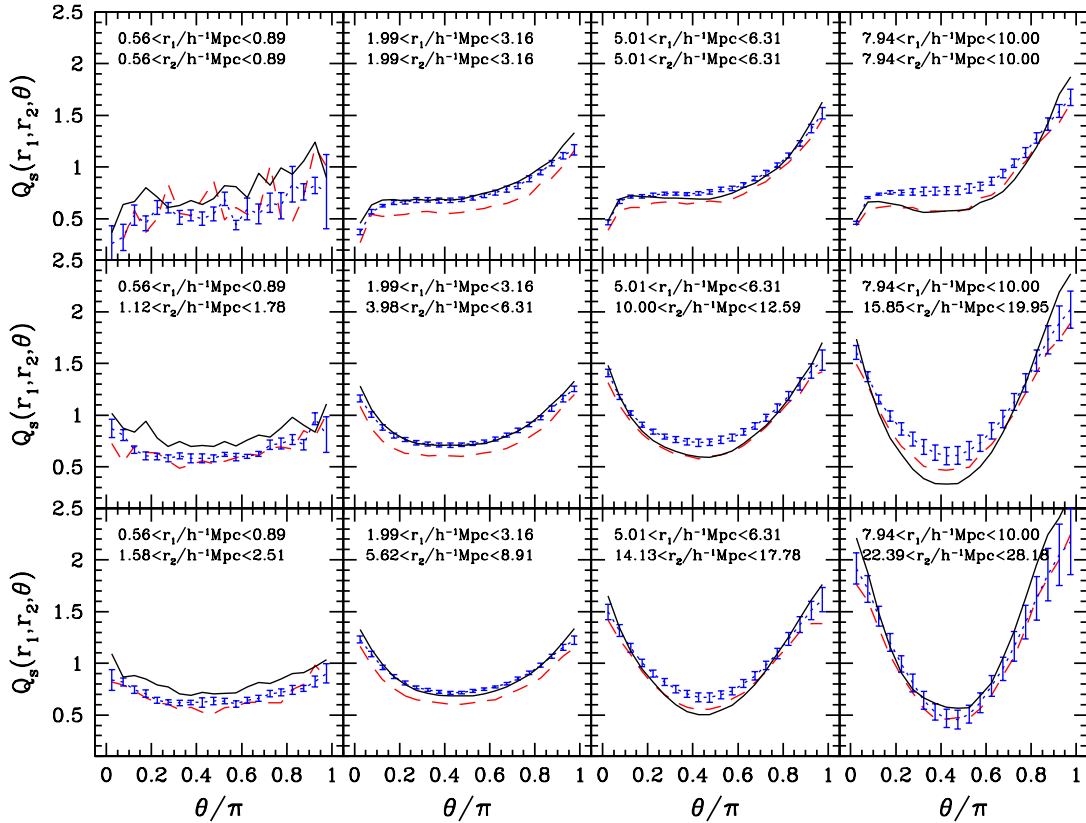


FIG. 6.— Redshift-space reduced 3PCF,  $Q_s$ , for different stellar-mass samples at various scales and triangle shapes. Lines of different colors denote different stellar samples, with the black solid, blue dotted, and red dashed lines for  $M_2$ ,  $M_3$ , and  $M_4$ , respectively. The errors are only shown for one sample for clarity. (A color version of this figure is available in the online journal.)

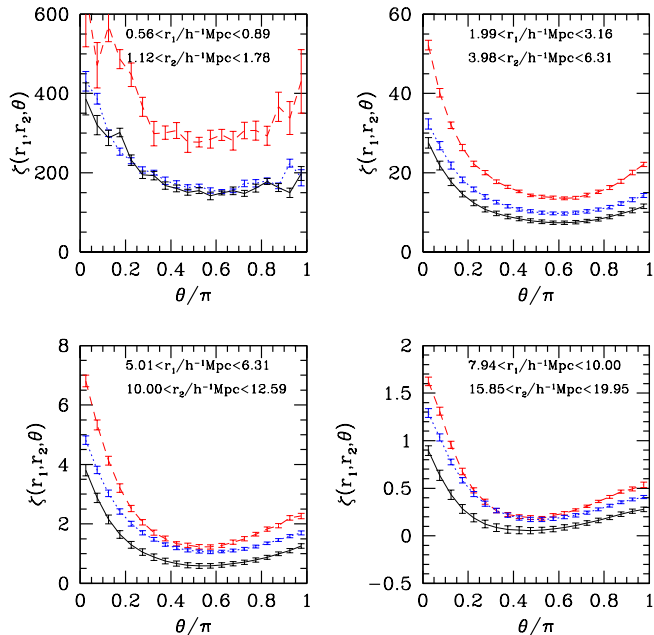


FIG. 7.— Redshift-space 3PCF,  $\zeta(r_1, r_2, \theta)$ , for different stellar-mass samples at various scales. The lines are the same as in Figure 6. Only the case of  $\bar{r}_2 = 2\bar{r}_1$  is shown. (A color version of this figure is available in the online journal.)

plying that the stellar-mass dependence of the reduced 3PCF is not significantly affected by the RSD effect. In Figure 9, we compare  $Q_s$  and  $Q_p$  for the sample of  $10.0 < \log(M_s) < 10.5$ . We find that  $Q_p$  generally has a weaker shape dependence than  $Q_s$ , which different from the conclusion of McBride et al. (2011a), who shows that the projected-space  $Q_p$  recovers more shape dependence that is lost in  $Q_s$  due to RSD. It is possible that the shape dependence shown in their figures is somewhat smoothed out by their choice of the parameterization  $(r_1, r_2, r_3)$ . Marin et al. (2008) compared the measurements of the reduced 3PCF in real and redshift spaces for scales down to  $r_1 = 1.5 h^{-1} \text{Mpc}$  using the  $N$ -body simulations. They found a significant configuration dependence of  $Q$  in real space and concluded that the RSDs attenuate the shape dependence of  $Q$ . Since the projected correlation function is directly related to the real-space correlation function (Jing & Börner 2004), the weaker shape dependence of  $Q_p$  seems to contradict the predictions from the simulations in real space. This could be caused by the possible selection effects or systematics in the survey that suppress the shape dependence in the projected space. We will study this further using mock galaxy catalogs in future work.

#### 4.2. Color Dependence

We show the color dependence of  $Q_s$  and  $Q_p$  for different stellar-mass samples in Figures 10 and 11. The red triangles and blue squares are for the red and blue galaxies defined in Section 2, respectively. The results for all the galaxies in the stellar-mass samples are also shown as black lines. We only display the results for the case of  $\bar{r}_2/\bar{r}_1 = 2$ . The measurement errors for the blue galaxies in the top right panels of Figures 10 and 11 are very large because of the shot-noise errors of small numbers of triplet counts at these small scales. The differences between the 3PCFs of the red and blue galaxies are

more significant for less massive samples and on smaller scales. For the most massive galaxy sample in the right panels of Figures 10 and 11, there is no significant dependence on color, considering the large errors on the measurements of blue galaxies. Although the fraction of red to blue galaxies changes with the stellar-mass subsamples considered, it only affects the shot-noise levels of the measurements of different color samples and should not change the color dependence of  $Q_s$  and  $Q_p$ .

Using high-resolution  $N$ -body simulations, Guo & Jing (2009b) demonstrate that Equation (12) can be applied to measure the linear and nonlinear galaxy bias even on small scales where the second-order perturbation theory fails and the bias factors become scale dependent. The red galaxies are found to have a higher clustering amplitude than the blue galaxies in the 2PCF measurements (Zehavi et al. 2005; Li et al. 2006a), i.e., red galaxies have a larger linear galaxy bias,  $b_1$ . For linear-bias models, we expect  $Q_s$  and  $Q_p$  for red galaxies to be somewhat smaller than those for blue galaxies, contrary to the results in Figures 10 and 11. This implies that the linear-bias model is not enough to describe the galaxy bias of different color samples, i.e., the nonlinear bias factor,  $b_2$ , would not be negligible and plays an important role in the modeling of the reduced 3PCF for galaxies of different colors. Considering that  $b_1$  and  $Q$  are both larger for red galaxies, we infer from Equation (12) that the nonlinear bias  $b_2$  of the red galaxies would also be larger than that of the blue ones. Because of the scale dependence of the bias factors, constant bias models are only accurate on large scales and precise measurements of the dark matter 3PCF is required for accurate estimation of the bias factors (Guo & Jing 2009a; Pollack et al. 2013). Comparing Figures 10 and 11, it seems that the RSD effect is stronger for the red galaxies, especially on small scales, while the blue galaxies suffer less from the RSD.

In the 2PCF, the differences between the clustering strength of the red and blue galaxies become smaller in more luminous galaxy samples and on larger scales (Li et al. 2006a). We also find a similar trend in  $Q_s$  and  $Q_p$ . In the bottom panels of Figures 10 and 11,  $Q_s$  and  $Q_p$  for the red and blue galaxies are more similar on large scales and in more massive galaxy samples. It implies that the galaxy bias factors would have less dependence on color for massive galaxies on large scales, which provides the opportunity to use massive galaxies irrespective of color to correctly measure the large-scale bias in galaxy redshift surveys.

Considering the significant differences of red and blue galaxies in the low-mass end, the 3PCF can provide powerful constraints to the formation and evolution of the low mass galaxies. The higher reduced 3PCF  $Q_s$  or  $Q_p$  for these low-mass red galaxies on small scales reflects the different distributions of red and blue galaxies within the dark matter halos. From the perspective of the halo model (see e.g., Fosalba et al. 2005), the small-scale contribution to the 3PCF mostly comes from the one-halo term where triplets of galaxies reside in the same halos. Since the red galaxies of such low stellar masses are mostly satellite galaxies in relatively massive halos and most of these blue galaxies are central galaxies (Li et al. 2007; Zehavi et al. 2011), the lack of one-halo central-satellite-satellite and satellite-satellite-satellite

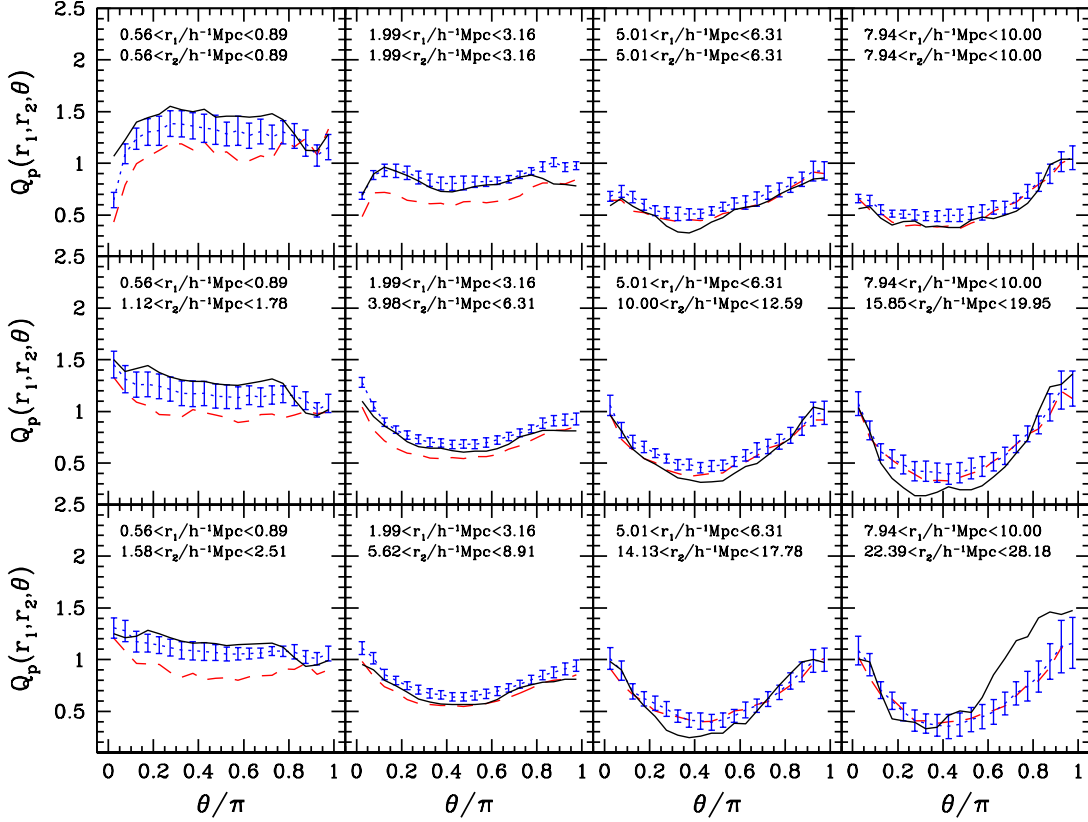


FIG. 8.— Same as in Figure 6, but for the projected-space reduced 3PCF,  $Q_p$ . (A color version of this figure is available in the online journal.)

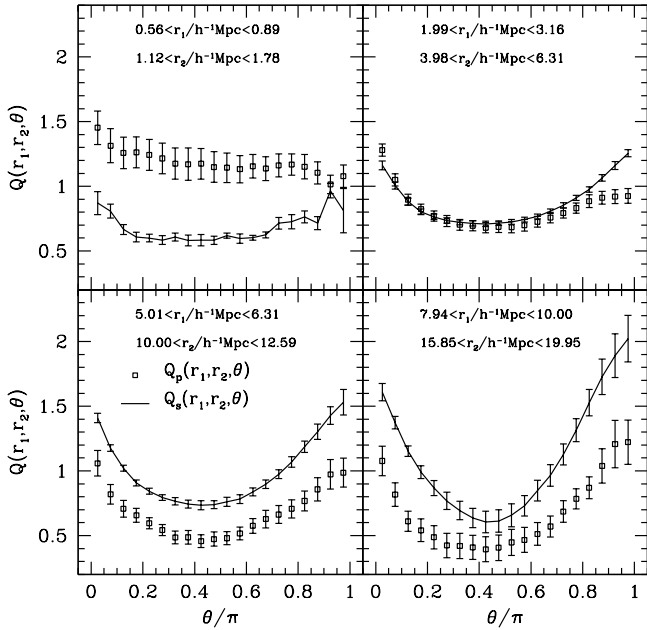


FIG. 9.— Comparison of the scale and shape dependence of  $Q_s$  (redshift space) and  $Q_p$  (projected space) for the stellar-mass sample of  $10.0 < \log(M_s) < 10.5$ . The points are for  $Q_p$  and lines for  $Q_s$ .

contributions from the blue galaxies results in the lower amplitudes of  $Q_s$  and  $Q_p$ . Similarly, the small differences of the reduced 3PCF for red and blue galaxies in

the high-stellar-mass samples reflect the similar satellite fractions of different colors. The clustering differences in the low-mass end could also relate to the different environments of the low-mass red and blue galaxies, since the red galaxies tend to populate denser regions (Hogg et al. 2003). We note that for low-mass samples, red galaxies have a stronger shape dependence than the blue galaxies, especially on large scales. This indicates that the low-mass red galaxies are more influenced by the large-scale structure and preferentially populate the filamentary structures.

## 5. CONCLUSIONS AND DISCUSSIONS

In this paper, we measure the stellar mass and color dependence of the galaxy 3PCF using the SDSS DR7 main sample galaxies in the redshift range of  $0.001 < z < 0.5$ . We also investigate the scale and shape dependence of the 3PCF for samples of different stellar mass and color in both redshift and projected spaces.

In the redshift space, the dependence of the reduced 3PCF,  $Q_s$ , on the stellar mass is very weak. Slightly stronger dependence on stellar mass shows up on small scales, where there is a trend that more massive galaxies have lower amplitudes of  $Q_s$ , consistent with the finding that more luminous galaxies have smaller  $Q_s$  (Jing & Börner 2004; McBride et al. 2011a). Such a behavior of  $Q_s$  can be qualitatively understood from the larger linear bias of more massive galaxies using the second-order perturbation theories. The reduced 3PCF,  $Q_s$ , is also dependent on the scale and shape of the triangle, which provides measurements of the 3D spatial

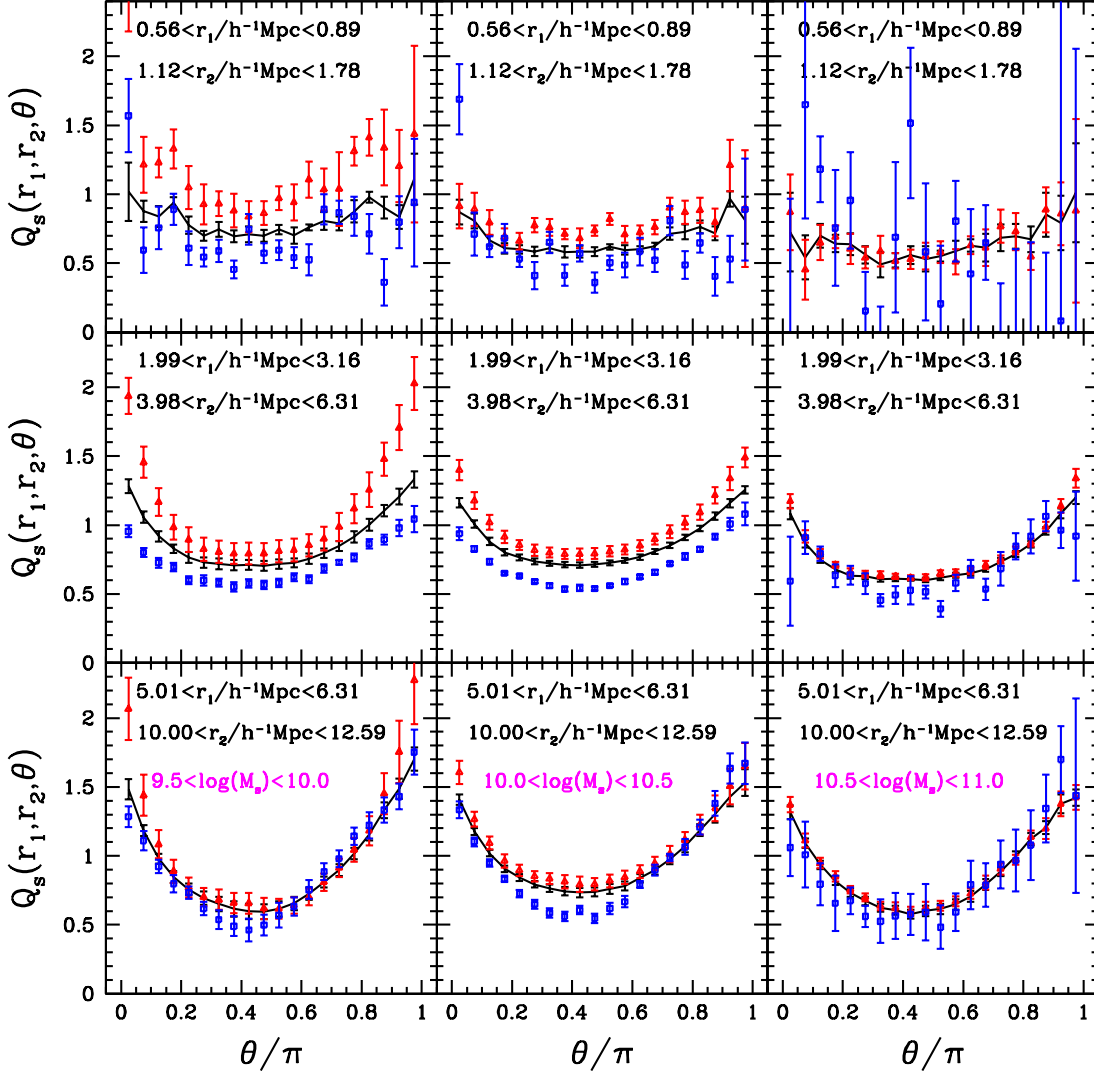


FIG. 10.— Redshift-space reduced 3PCF,  $Q_s$ , for different color samples at different stellar mass and scales. The left, middle, and right panels are for the samples of  $9.5 < \log M_s < 10$ ,  $10 < \log M_s < 10.5$ , and  $10.5 < \log M_s < 11$ , respectively. The red triangles and blue squares are for red and blue galaxies defined in Section 2, respectively. The results for all the galaxies in the stellar-mass samples are shown as black lines for comparison. We only display the results for  $\bar{r}_2/\bar{r}_1 = 2$ . (A color version of this figure is available in the online journal.)

distribution in the galaxies. We find that the shape dependence of  $Q_s$  is stronger on larger scales, reflecting the fact that the filamentary structures dominate the large-scale distribution. More massive galaxies show weaker shape dependence of  $Q_s$ , which is possibly resulting from the high occupancy of low-mass galaxies in the filamentary structures. The reduced 3PCF,  $Q_s$ , only has weak shape dependence on small scales, regardless of the stellar mass, meaning that the hierarchical clustering model  $\zeta \propto \xi^2$  would be more accurate on these small scales.

To study the effect of RSD, we also measure the similar dependence of the projected-space reduced 3PCF  $Q_p$  on stellar mass, scale, and the triangle shape. We find no strong dependence of  $Q_p$  on the stellar mass at different scales and triangle shapes, as in the redshift space. It means that the weak stellar-mass dependence is not caused by the RSD effect. Weaker shape dependence is found for  $Q_p$  than that of redshift-space 3PCF  $Q_s$ , which is different from the expectation that RSD attenuates the shape dependence of the reduced 3PCF. We will explore

this effect in more detail using mock galaxy catalogs in future work.

We also investigate the color dependence of  $Q_s$  and  $Q_p$  for different stellar mass samples. In redshift space, the color dependence is stronger for low-mass galaxies and on small scales, reflecting the different distributions of low-mass red and blue galaxies in the small-scale structures. The low-mass red galaxies have higher 2PCF clustering amplitudes and also higher  $Q_s$  values, which indicates that the linear bias models are not sufficient to predict the 3PCF distribution of various color samples. The higher amplitude of  $Q_s$  for red galaxies implies that the red galaxies reside in denser environments than the blue galaxies. Red galaxies display stronger shape dependence than blue galaxies in the low-mass samples on large scales, which means that the low-mass red galaxies tend to populate the filamentary structures. The high-mass red and blue galaxies generally show very similar amplitudes and shape dependence of  $Q_s$  on all scales probed, indicating their similar spatial distributions.



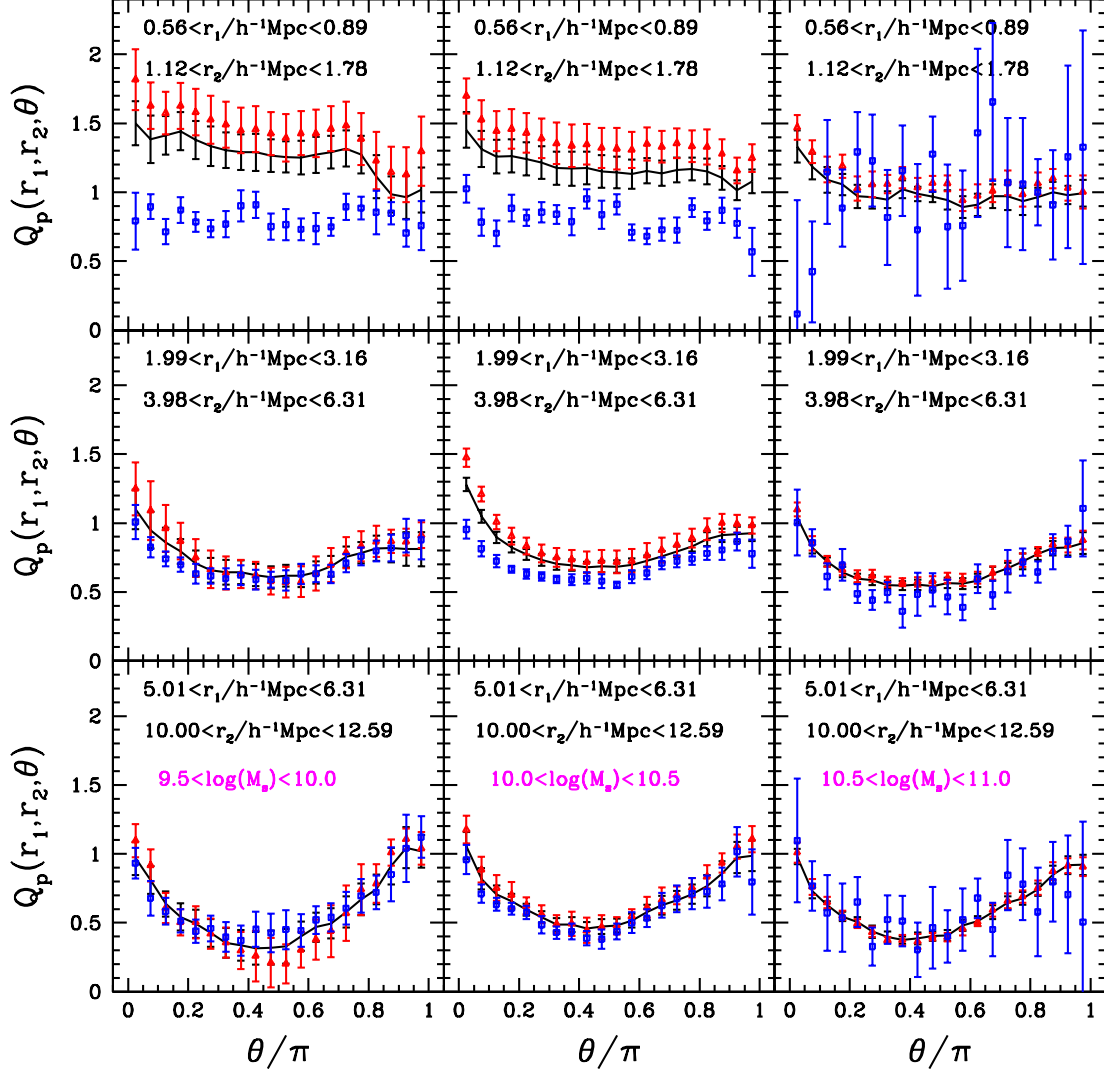


FIG. 11.— Same as in Figure 10, but for the projected-space reduced 3PCF,  $Q_p$ . (A color version of this figure is available in the online journal.)

In the projected space, the similar differences between the  $Q_p$  for red and blue galaxies are still significant for low-mass galaxies. But such differences are smaller compared to those in the redshift space, especially for the red galaxies. This is an indication of stronger RSD effects for the low-mass red galaxy distribution. The behavior of the high-mass red and blue galaxies are still similar as in the redshift space.

From the conclusions above, we can have a clearer picture of how the 3PCF helps understand the galaxy spatial distribution and their formation and evolution. For example, from the reduced 3PCF of the low-mass red galaxies, we conclude that on large scales these galaxies preferentially populate the filamentary structures. On small scales, they are more clustered than the blue galaxies of similar masses and populate denser regions. The failure of the linear bias model for the color samples is also consistent with the fact that most of these low-mass red galaxies are satellite galaxies and their nonlinear evolution is important.

Since the different behaviors in the spatial clustering of

3PCF reflect the different formation and merger history of galaxies, we will use the 3PCF measurements in this work to test the galaxy formation and evolution models using detailed halo occupation models and also connect the relation of galaxy stellar masses and host halo masses in our future work. The study of the stellar mass dependence of the 3PCF will help further constrain the galaxy formation and evolution models when combined with the information of the star formation rates, merger histories, and even the active galactic nucleus feedback of the different stellar mass samples in the semi-analytical models.

We thank the anonymous referee for the helpful suggestions that significantly improve the paper. This work is supported by NSFC (no. 11173045, no. 11233005, no. 11320101002, no. 11325314) and the CAS/SAFEA International Partnership Program for Creative Research Teams (KJCX2-YW-T23). HG was supported by NSF grant AST-0907947. CL acknowledges the support of the 100 Talents Program of the Chinese Academy of Sciences (CAS), Shanghai Pujiang Program (no. 11PJ1411600)

and the exchange program between the Max Planck Society and the CAS.

Funding for the SDSS and SDSS-II has been provided by the Alfred P. Sloan Foundation, the Participating Institutions, the National Science Foundation, the U.S. Department of Energy, the National Aeronautics and Space Administration, the Japanese Monbukagakusho, the Max Planck Society, and the Higher Education Funding Council for England. The SDSS Web Site is <http://www.sdss.org/>.

The SDSS is managed by the Astrophysical Research Consortium for the Participating Institutions. The Participating Institutions are the American Museum of Natural History, Astrophysical Institute Potsdam,

University of Basel, University of Cambridge, Case Western Reserve University, University of Chicago, Drexel University, Fermilab, the Institute for Advanced Study, the Japan Participation Group, Johns Hopkins University, the Joint Institute for Nuclear Astrophysics, the Kavli Institute for Particle Astrophysics and Cosmology, the Korean Scientist Group, the Chinese Academy of Sciences (LAMOST), Los Alamos National Laboratory, the Max-Planck-Institute for Astronomy (MPIA), the Max-Planck-Institute for Astrophysics (MPA), New Mexico State University, Ohio State University, University of Pittsburgh, University of Portsmouth, Princeton University, the United States Naval Observatory, and the University of Washington.

#### REFERENCES

- Abazajian, K. N., Adelman-McCarthy, J. K., Agüeros, M. A., et al. 2009, *ApJS*, 182, 543
- Bardeen, J. M., Bond, J. R., Kaiser, N., & Szalay, A. S. 1986, *ApJ*, 304, 15
- Beisbart, C., & Kerscher, M. 2000, *ApJ*, 545, 6
- Bell, E. F., McIntosh, D. H., Katz, N., & Weinberg, M. D. 2003, *ApJS*, 149, 289
- Benoist, C., Maurogordato, S., da Costa, L. N., Cappi, A., & Schaeffer, R. 1996, *ApJ*, 472, 452
- Bernardeau, F., Colombi, S., Gaztañaga, E., & Scoccimarro, R. 2002, *PhR*, 367, 1
- Blanton, M. R., & Roweis, S. 2007, *AJ*, 133, 734
- Blanton, M. R., Schlegel, D. J., Strauss, M. A., et al. 2005, *AJ*, 129, 2562
- Boerner, G., Mo, H., & Zhou, Y. 1989, *A&A*, 221, 191
- Chabrier, G. 2003, *PASP*, 115, 763
- Colless, M., Dalton, G., Maddox, S., et al. 2001, *MNRAS*, 328, 1039
- Cooray, A., & Sheth, R. 2002, *PhR*, 372, 1
- Coupon, J., Kilbinger, M., McCracken, H. J., et al. 2012, *A&A*, 542, A5
- Croton, D. J., Springel, V., White, S. D. M., et al. 2006, *MNRAS*, 365, 11
- Davis, M., Efstathiou, G., Frenk, C. S., & White, S. D. M. 1985, *ApJ*, 292, 371
- Davis, M., & Geller, M. J. 1976, *ApJ*, 208, 13
- Davis, M., Meiksin, A., Strauss, M. A., da Costa, L. N., & Yahil, A. 1988, *ApJL*, 333, L9
- Einasto, M. 1991, *MNRAS*, 252, 261
- Fosalba, P., Pan, J., & Szapudi, I. 2005, *ApJ*, 632, 29
- Fry, J. N., & Gaztanaga, E. 1993, *ApJ*, 413, 447
- Gaztañaga, E., Norberg, P., Baugh, C. M., & Croton, D. J. 2005, *MNRAS*, 364, 620
- Gaztañaga, E., & Scoccimarro, R. 2005, *MNRAS*, 361, 824
- Gaztanaga, E., & Frieman, J. A. 1994, *ApJ*, 437, L13
- Groth, E. J., & Peebles, P. J. E. 1977, *ApJ*, 217, 385
- Guo, H., & Jing, Y. P. 2009a, *ApJ*, 698, 479
- Guo, H., & Jing, Y. P. 2009b, *ApJ*, 702, 425
- Guo, H., Zehavi, I., & Zheng, Z. 2012, *ApJ*, 756, 127
- Guo, H., Zehavi, I., Zheng, Z., et al. 2013, *ApJ*, 767, 122
- Guzzo, L., Strauss, M. A., Fisher, K. B., Giovanelli, R., & Haynes, M. P. 1997, *ApJ*, 489, 37
- Hamilton, A. J. S. 1988, *ApJ*, 331, L59
- Hogg, D. W., Blanton, M. R., Eisenstein, D. J., et al. 2003, *ApJ*, 585, L5
- Jing, Y. P., & Börner, G. 1998, *ApJ*, 503, 37
- Jing, Y. P., & Börner, G. 2004, *ApJ*, 607, 140
- Kaiser, N. 1984, *ApJ*, 284, L9
- Kauffmann, G., Heckman, T. M., White, S. D. M., et al. 2003, *MNRAS*, 341, 54
- Kayo, I., Suto, Y., Nichol, R. C., et al. 2004, *PASJ*, 56, 415
- Kulkarni, G. V., Nichol, R. C., Sheth, R. K., et al. 2007, *MNRAS*, 378, 1196
- Landy, S. D., & Szalay, A. S. 1993, *ApJ*, 412, 64
- Li, C., Jing, Y. P., Kauffmann, G., et al. 2007, *MNRAS*, 376, 984
- Li, C., Kauffmann, G., Fu, J., et al. 2012a, *MNRAS*, 424, 1471
- Li, C., Kauffmann, G., Jing, Y. P., et al. 2006a, *MNRAS*, 368, 21
- Li, C., Kauffmann, G., Wang, L., et al. 2006b, *MNRAS*, 373, 457
- Li, C., Wang, L., & Jing, Y. P. 2013, *ApJ*, 762, L7
- Li, C., & White, S. D. M. 2009, *MNRAS*, 398, 2177
- Li, C., White, S. D. M., Chen, Y., et al. 2012b, *MNRAS*, 419, 1557
- Loveday, J., Maddox, S. J., Efstathiou, G., & Peterson, B. A. 1995, *ApJ*, 442, 457
- Marín, F. 2011, *ApJ*, 737, 97
- Marín, F. A., Blake, C., Poole, G. B., et al. 2013, *MNRAS*, 432, 2654
- Marín, F. A., Wechsler, R. H., Frieman, J. A., & Nichol, R. C. 2008, *ApJ*, 672, 849
- McBride, C. K., Connolly, A. J., Gardner, J. P., et al. 2011a, *ApJ*, 726, 13
- McBride, C. K., Connolly, A. J., Gardner, J. P., et al. 2011b, *ApJ*, 739, 85
- Nichol, R. C., Sheth, R. K., Suto, Y., et al. 2006, *MNRAS*, 368, 1507
- Nishimichi, T., Kayo, I., Hikage, C., et al. 2007, *PASJ*, 59, 93
- Norberg, P., Baugh, C. M., Hawkins, E., et al. 2001, *MNRAS*, 328, 64
- Pan, J., & Szapudi, I. 2005, *MNRAS*, 362, 1363
- Park, C., Vogeley, M. S., Geller, M. J., & Huchra, J. P. 1994, *ApJ*, 431, 569
- Percival, W. J., Reid, B. A., Eisenstein, D. J., et al. 2010, *MNRAS*, 401, 2148
- Pollack, J. E., Smith, R. E., & Porciani, C. 2013, *arXiv:1309.0504*
- Ross, A. J., & Brunner, R. J. 2009, *MNRAS*, 399, 878
- Ross, N. P., Shanks, T., Cannon, R. D., et al. 2008, *MNRAS*, 387, 1323
- Scoccimarro, R., Couchman, H. M. P., & Frieman, J. A. 1999, *ApJ*, 517, 531
- Scoccimarro, R., Sheth, R. K., Hui, L., & Jain, B. 2001, *ApJ*, 546, 20
- Skibba, R., Sheth, R. K., Connolly, A. J., & Scranton, R. 2006, *MNRAS*, 369, 68
- Springel, V., White, S. D. M., Jenkins, A., et al. 2005, *Natur*, 435, 629
- Swanson, M. E. C., Tegmark, M., Blanton, M., & Zehavi, I. 2008, *MNRAS*, 385, 1635
- Szapudi, S., & Szalay, A. S. 1998, *ApJ*, 494, L41
- Tegmark, M., Blanton, M. R., Strauss, M. A., et al. 2004, *ApJ*, 606, 702
- Verde, L., Heavens, A. F., Percival, W. J., et al. 2002, *MNRAS*, 335, 432
- Wang, L., & Jing, Y. P. 2010, *MNRAS*, 402, 1796
- Wang, Y., Yang, X., Mo, H. J., & van den Bosch, F. C. 2007, *ApJ*, 664, 608
- Watson, D. F., Berlind, A. A., & Zentner, A. R. 2011, *ApJ*, 738, 22
- White, S. D. M., & Rees, M. J. 1978, *MNRAS*, 183, 341
- White, S. D. M., Tully, R. B., & Davis, M. 1988, *ApJ*, 333, L45
- York, D. G., Adelman, J., Anderson, J. E., Jr., et al. 2000, *AJ*, 120, 1579
- Zehavi, I., Blanton, M. R., Frieman, J. A., et al. 2002, *ApJ*, 571, 172
- Zehavi, I., Zheng, Z., Weinberg, D. H., et al. 2005, *ApJ*, 630, 1

Zehavi, I., Zheng, Z., Weinberg, D. H., et al. 2011, ApJ, 736, 59  
Zheng, Z. 2004, ApJ, 614, 527  
Zheng, Z., Coil, A. L., & Zehavi, I. 2007a, ApJ, 667, 760

Zheng, Z., Coil, A. L., & Zehavi, I. 2007b, ApJ, 667, 760  
Zheng, Z., Zehavi, I., Eisenstein, D. J., Weinberg, D. H., & Jing,  
Y. P. 2009, ApJ, 707, 554